Draft version February 5, 2008
Preprint typeset using LaTeX style emulateapj v. 10/09/06

arXiv:astro-ph/0607652v3 8 May 2007

THE MAXIMUM B-MODE POLARIZATION OF THE COSMIC MICROWAVE BACKGROUND FROM INHOMOGENEOUS REIONIZATION

Michael J. Mortonson[1,2] and Wayne Hu[1,3]
[1]Kavli Institute for Cosmological Physics, Enrico Fermi Institute, University of Chicago, Chicago, IL 60637
[2]Department of Physics, University of Chicago, Chicago, IL 60637
[3]Department of Astronomy and Astrophysics, University of Chicago, Chicago, IL 60637
Draft version February 5, 2008

ABSTRACT

We compute the B-mode polarization power spectrum of the CMB from an epoch of inhomogeneous reionization, using a simple model in which H II regions are represented by ionized spherical bubbles with a log normal distribution of sizes whose clustering properties are determined by large-scale structure. Both the global ionization fraction and the characteristic radius of H II regions are allowed to be free functions of redshift. Models that would produce substantial contamination to degree scale gravitational wave B-mode measurements have power that is dominated by the shot noise of the bubbles. Rare bubbles of $\gtrsim 100$ Mpc at $z > 20$ can produce signals that in fact exceed the B-modes from gravitational lensing and are comparable to the maximal allowed signal of gravitational waves ($\sim 0.1\ \mu$K) while still being consistent with global constraints on the total optical depth. Even bubbles down to 20 Mpc at $z \sim 15$, or 40 Mpc at $z \sim 10$ can be relevant ($0.01\ \mu$K) once the lensing signal is removed either statistically or directly. However, currently favored theoretical models that have ionization bubbles that only grow to such sizes at the very end of a fairly prompt and late reionization produce signals which are at most at these levels.

Subject headings: cosmic microwave background — cosmology: theory — large-scale structure of universe

1. INTRODUCTION

The polarization of the cosmic microwave background (CMB) can be decomposed into two components, E-modes and B-modes, which are geometrically distinct but non-local combinations of the Stokes parameters Q and U. The two modes are distinguished by the relationship between the direction of polarization and its spatial gradients. In linear perturbation theory, both scalar and tensor perturbations contribute to the E-modes, but scalar perturbations do not produce B-modes (Kamionkowski et al. 1997; Seljak & Zaldarriaga 1997). This fact makes observation of the CMB B-modes an ideal way to detect the tensor perturbations from gravitational waves generated during inflation. Detection of gravitational waves would be strong evidence in favor of inflation, would determine the energy scale of inflation, and would help constrain models of inflation (see e.g. Gold & Albrecht 2003; Verde et al. 2006, for recent assessments). This detection is the goal of a concerted experimental effort currently underway (Bock et al. 2006).

Beyond linear perturbations, scalar density fluctuations can generate B-modes. For example, gravitational lensing spatially distorts the polarization field in a manner that is independent of its orientation and hence generates B-modes from the intrinsic E-modes from recombination (Zaldarriaga & Seljak 1998). Lensing places a fundamental limitation on the detection of inflationary gravitational waves that is not far in energy scale from current limits (e.g., Page et al. 2006) if only polarization power spectra are measured. Fortunately, with high signal-to-noise, high resolution polarization maps, delensing of the polarization field is in principle possible (Hu & Okamoto 2002; Hirata & Seljak 2003) and may improve limits by an order of magnitude or more in polarization power (Knox & Song 2002; Kesden et al. 2002; Seljak & Hirata 2004). In addition, predictions for the gravitational lensing B-modes are highly accurate and hence their contamination to a power spectrum measurement may be subtracted to within a few percent for a cosmic variance limited experiment.

More worrying would be cosmological B-mode sources that cannot be accurately modelled theoretically. As pointed out in Hu (2000), inhomogeneities in the free electron density during reionization will generate B-modes through Thomson scattering. Fluctuations in the local ionization fraction during an extended epoch of reionization are in fact expected. Current observations show evidence for an extended epoch of reionization that ends at redshift $z \sim 6$ and begins at $z \gtrsim 10$ (Fan et al. 2006). Because reionization is a gradual process and the sources of ionizing radiation are clustered, the distribution of neutral and ionized hydrogen during the epoch of reionization is expected to be highly inhomogeneous (e.g., Barkana & Loeb 2001).

Previous studies of B-modes generated by inhomogeneous (or "patchy") reionization have shown that they are negligible compared with B-modes from lensing at scales relevant for gravitational waves if the ionized regions are small and uncorrelated with each other and reionization is prompt (Hu 2000; Weller 1999). Correlations between ionized regions can boost the signal but not substantially (Knox et al. 1998; Santos et al. 2003; Baumann et al. 2003). However, because reionization is a highly uncertain process, it has not been possible to rule it out as a source of significant B-modes when these conditions are violated.

In this paper, we take a phenomenological approach to the study of B-mode generation from inhomogeneous reionization to bound the possible contamination to grav-

itational wave studies. We limit our considerations to models that satisfy observational bounds on the total optical depth $\tau_* = 0.09 \pm 0.03$ (Spergel et al. 2006). We fix the other cosmological parameters to also be consistent with the 3-year WMAP results: Hubble constant $H_0 = 100h$ km s^{-1} Mpc^{-1} with $h = 0.73$, matter density $\Omega_m h^2 = 0.128$, baryon density $\Omega_b h^2 = 0.0223$, flat spatial geometry $\Omega_K = 0$, CMB temperature $T_{\rm CMB} = 2.725$ K, primordial helium fraction $Y_p = 0.24$, scalar index $n_S = 0.958$, and amplitude $\sigma_8 = 0.76$.

Our approach should be contrasted with studies of physically motivated models of reionization (Liu et al. 2001; Zahn et al. 2005). The advantage of our approach is its ability to describe a wide variety of reionization scenarios with relatively few phenomenological parameters. The parameters that are required to generate substantial B-modes can then be compared with predictions from physical models.

The outline of the paper is as follows. In Section 2, we introduce a phenomenological model of inhomogeneous reionization that incorporates several free functions of redshift. We parameterize these functions in Section 3 in a manner which highlights the phenomenology of the B-modes discussed in Section 4. We discuss observational and theoretical bounds on the parameter space in Section 5 and conclude in Section 6.

2. INHOMOGENEOUS REIONIZATION MODELS

Reionization generates polarization by Thomson scattering of anisotropic radiation coming from recombination. If the ionized hydrogen is homogeneous, the scalar quadrupole temperature anisotropy creates only E-mode polarization. Inhomogeneities break this symmetry and generate B-mode polarization. Under the Limber approximation, valid for multipoles $\ell \gg 10$, the B-mode power spectrum is related to the power spectrum of the ionized hydrogen $P_{\delta_{\rm HII}}(k,z)$ as (Hu 2000)

$$C_\ell^B = \frac{3\sigma_T^2 n_{p,0}^2}{100}\int_{z_f}^{z_i}\frac{dz(1+z)^4}{H(z)D_A^2(z)}e^{-2\tau(z)}Q_{\rm rms}^2(z) \times P_{\delta_{\rm HII}}(k=\ell/D_A,z), \quad (1)$$

where σ_T is the Thomson scattering cross section, $n_{p,0}$ is the present number density of protons, z_i and z_f are the redshifts at the beginning and end of the epoch of reionization, $H(z)$ is the Hubble parameter, $D_A(z)$ is the angular diameter distance, $\tau(z)$ is the optical depth out to redshift z, and $Q_{\rm rms}^2(z)$ is the variance of the quadrupole. We define the ionization fraction to equal 1 when both hydrogen and helium are fully ionized, so $n_{p,0} = (1-Y_p/2)n_{b,0}$. In the fiducial model $Q_{\rm rms} \approx 18\,\mu$K at the redshifts of interest. We often use the notation

$$\mathcal{C}_\ell^B \equiv \ell(\ell+1)C_\ell^B/2\pi\,, \quad (2)$$

for the power per logarithmic interval in multipole.

To evaluate equation (1), we need a model for inhomogeneous reionization. Because we are interested in exploring what types of ionization histories generate maximal amounts of B-modes, we adopt the phenomenological parameterization of Wang & Hu (2006) instead of a more physically motivated one (e.g., Furlanetto et al. 2004).

In this parameterization, each ionized H II region is a spherical bubble of radius R with full ionization inside, and neutral hydrogen outside. We generalize the parameterization of Wang & Hu (2006) to describe the power spectrum of H II regions rather than H I regions and allow the H II bubbles to have a distribution of radii, $P(R)$, that can evolve with redshift. Note that we suppress the redshift arguments to functions such as $P(R)$ where no confusion will arise. The physical mechanisms of reionization, including what the ionizing sources are and how efficiently they can ionize neutral gas surrounding them, are left unspecified. Therefore not all of the parameter space available corresponds to currently favored, or even physically plausible, models.

In Section 2.1 we describe the basic features of the model and the relationship between the bubble distribution and mean ionization. In Section 2.2 we show how the ionization history and bubble radius distribution determines the power spectrum of the ionized hydrogen. Finally in Section 2.3 we explore the impact of the width of the distribution on the power spectrum.

2.1. *Mean Ionization*

We assume that H II bubbles populate a large volume V_0 as a Poisson process with fluctuating mean (Valageas et al. 2001; Furlanetto et al. 2004; Wang & Hu 2006). In addition we allow the bubbles to have an arbitrary distribution of radii $P(R)$. The volume of each bubble is $V_b(R) = 4\pi R^3/3$. Then the ionization fraction is

$$\langle x(\mathbf{r})\rangle_{\rm P} = 1 - \exp\left[-\int dR\frac{dn_b}{dR}V_b(R)\right], \quad (3)$$

where $dn_b/dR = n_b(\mathbf{r})P(R)$ and $n_b(\mathbf{r})$ is the comoving bubble number density, and the subscript P denotes averaging over the Poisson process.

The average ionization fraction in the volume V_0 is

$$x_e = 1 - \frac{1}{V_0}\int_{V_0} d^3r \exp\left[-\int dR\frac{dn_b}{dR}V_b(R)\right]. \quad (4)$$

We assume the number density of bubbles fluctuates as a biased tracer of the large scale structure with bubble bias $b(R)$:

$$\frac{dn_b}{dR} = \frac{d\bar{n}_b}{dR}\left[1 + b(R)\delta_W(\mathbf{r})\right], \quad (5)$$

where $\delta_W(\mathbf{r}) = \int d^3r'\delta(\mathbf{r}')W_R(\mathbf{r}-\mathbf{r}')$ is the overdensity δ smoothed with a top-hat window function

$$W_R(k) = \frac{3}{(kR)^3}[\sin(kR) - kR\cos(kR)]. \quad (6)$$

In our model, we assume that the bubble bias is independent of R, $b(R) = b$ for simplicity.

Using equation (5) and expanding the exponential in equation (4), we find that the average number density, bubble volume and ionization fraction are related by

$$1 - x_e \approx \frac{e^{-\bar{n}_b\langle V_b\rangle}}{V_0}\int_{V_0} d^3r\left[1 - b\int dR\frac{d\bar{n}_b}{dR}V_b(R)\delta_W(\mathbf{r})\right] = e^{-\bar{n}_b\langle V_b\rangle}, \quad (7)$$

where we define

$$\langle V_b\rangle \equiv \int dR\ P(R)V_b(R), \quad (8)$$

and assume $\int_{V_0} d^3r\delta_W(\mathbf{r}) = 0$ for a sufficiently large volume. Therefore any two of $\{x_e, \bar{n}_b, \langle V_b\rangle\}$ specifies the mean ionization model.

2.2. *Ionized Hydrogen Power Spectrum*

The ionization field can be written as $x(\mathbf{r}) = x_e + \delta x(\mathbf{r})$, where x_e is the spatially averaged ionization fraction of equation (7). The ionized hydrogen perturbations have contributions from both ionization fluctuations δx and hydrogen overdensities δ (Hu 2000)

$$\delta_{\rm HII}(\mathbf{r}) = \delta x(\mathbf{r}) + [x_e + \delta x(\mathbf{r})]\delta(\mathbf{r}). \quad (9)$$

The 2-point correlation function of ionized hydrogen, $\xi_{\delta_{\rm HII}\delta_{\rm HII}}(r) = \langle \delta_{\rm HII}(\mathbf{r}_1)\delta_{\rm HII}(\mathbf{r}_2)\rangle$ where $r = |\mathbf{r}_1 - \mathbf{r}_2|$, is (Furlanetto et al. 2004)

$$\begin{aligned}\xi_{\delta_{\rm HII}\delta_{\rm HII}}(r) =& \xi_{\delta x\delta x}(r) + x_e^2\xi_{\delta\delta}(r) \\ &+\xi_{\delta x\delta\ \delta x\delta}(r) + 2x_e\xi_{\delta x\delta}(r),\end{aligned} \quad (10)$$

neglecting terms that are higher order in δ and δx (except $\xi_{\delta x\delta\ \delta x\delta}$, which turns out to be important to this order in the perturbations). The H II power spectrum is the Fourier transform of the correlation function,

$$P_{\delta_{\rm HII}}(k) = \int d^3r\ e^{i\mathbf{k}\cdot\mathbf{r}}\xi_{\delta_{\rm HII}\delta_{\rm HII}}(r). \quad (11)$$

Following Wang & Hu (2006), we compute the correlation functions in equation (10) by separating the contributions from one-bubble and two-bubble correlations, analogous to the halo model (see Cooray & Sheth 2002, for a review).

2.2.1. *Two-bubble terms*

For the two-bubble contribution to the two-point H II correlation function, the term $\xi^{2b}_{\delta x\delta\ \delta x\delta}$ is higher order than the other terms and can be dropped (Furlanetto et al. 2004). We choose to include the density correlation term $x_e^2\xi_{\delta\delta}$ with the two-bubble terms due to their joint dependence on the matter power spectrum $P(k)$. The remaining two-bubble terms in the H II power spectrum are $P^{2b}_{\delta x\delta x}(k)$ and $P^{2b}_{\delta x\delta}(k)$. To find these terms, we need an expression for $\delta x(\mathbf{r})$ that accounts for the clustering of H II regions through the bubble bias b.

Expanding the exponential in the Poisson-averaged ionization fraction equation (3) gives

$$\begin{aligned}\langle x(\mathbf{r})\rangle_{\rm P} &= 1 - e^{-\bar{n}_b\langle V_b\rangle}\left[1 - b\int dR\ \bar{n}_b P(R)V_b(R)\delta_W(\mathbf{r})\right] \\ &= x_e + (1-x_e)\bar{n}_b b\int dR\ P(R)V_b(R)\delta_W(\mathbf{r}), \end{aligned} \quad (12)$$

so the ionization fraction perturbation is

$$\begin{aligned}\langle\delta x(\mathbf{r})\rangle_{\rm P} &= \langle x(\mathbf{r})\rangle_{\rm P} - x_e \\ &= -\frac{(1-x_e)\ln(1-x_e)}{\langle V_b\rangle} b\int dR\ P(R)V_b(R)\delta_W(\mathbf{r}).\end{aligned} \quad (13)$$

Using this expression for δx, we can find the correlations of δx with δx, and δx with δ. The Fourier transforms of these correlation functions are

$$P^{2b}_{\delta x\delta x}(k) = [(1-x_e)\ln(1-x_e)b\langle W_R(k)\rangle]^2\ P(k), \quad (14)$$

$$P^{2b}_{\delta x\delta}(k) = -(1-x_e)\ln(1-x_e)b\langle W_R(k)\rangle P(k), \quad (15)$$

where $P(k) = P_{\delta\delta}(k)$ is the matter power spectrum, and the two-bubble window function averaged over the bubble radius distribution is defined as

$$\langle W_R(k)\rangle = \frac{1}{\langle V_b\rangle}\int dR\ V_b(R)P(R)W_R(k), \quad (16)$$

where $W_R(k)$ is the Fourier transform of the real-space top-hat window of equation (6).

The total two-bubble contribution to the power spectrum comes from combining the terms in equations (14) and (15) with the density fluctuation term $P(k)$, with coefficients as given by equation (10):

$$P^{2b}_{\delta_{\rm HII}}(k) = [(1-x_e)\ln(1-x_e)b\langle W_R(k)\rangle - x_e]^2\ P(k). \quad (17)$$

Finally to complete the description we need a model for the bubble bias b. We assume that the bubbles are centered on dark matter halos so that the bias of the central halo determines the bubble bias. Specifically, we match the desired number density of H II bubbles to the number density of halos above a mass threshold $M_{\rm th}$

$$\bar{n}_b = \int_{M_{\rm th}}^{\infty}\frac{dM}{M}\frac{dn_h}{d\ln M}, \quad (18)$$

where $dn_h/d\ln M$ is the halo mass function. In a physical model $M_{\rm th}$ might be associated with the threshold mass for collapse determined by cooling via atomic hydrogen. We use the Sheth & Tormen (1999) mass function for $dn_h/d\ln M$. The bubbles are then correlated according to the matter power spectrum but with a bias,

$$b = \frac{1}{\bar{n}_b}\int_{M_{\rm th}}^{\infty}\frac{dM}{M}b_h(M)\frac{dn_h}{d\ln M}, \quad (19)$$

where the bias of dark matter halos b_h is given by the Sheth & Tormen (1999) form. Note that this association with dark matter halos is only necessary for modelling the two bubble correlations. For much of the parameter space of interest, the one halo term dominates and its contributions are independent of this association.

2.2.2. *One-bubble terms*

In the one-bubble regime, we can neglect $\xi^{1b}_{\delta x\delta}$ in equation (10) because we assume complete ionization inside bubbles and complete neutrality outside (Wang & Hu 2006). The $\xi_{\delta\delta}$ term in $\xi_{\delta_{\rm HII}\delta_{\rm HII}}$ is already included in the two-bubble contribution to the power spectrum, so only the first and third terms in equation (10) remain. For our purposes, the main contribution from $\xi^{1b}_{\delta x\delta\ \delta x\delta}$ can be approximated by $\xi^{1b}_{\delta x\delta x}\xi_{\delta\delta}$ (Furlanetto et al. 2004; Wang & Hu 2006).

The two-point correlation of the total ionization fraction in the one-bubble regime can be written (Gruzinov & Hu 1998)

$$\begin{aligned}\langle x(\mathbf{r}_1)x(\mathbf{r}_2)\rangle =& x_e^2 + \xi^{1b}_{\delta x\delta x}(r) \\ =& x_e P_{2|1}(r) + x_e^2(1 - P_{2|1}(r)),\end{aligned} \quad (20)$$

where $P_{2|1}(r)$ is the probability of the point $\mathbf{r}_2$ being ionized (in the same bubble as $\mathbf{r}_1$) given that $\mathbf{r}_1$ is ionized, and $r = |\mathbf{r}_1 - \mathbf{r}_2|$. The first term is the probability that both points are ionized in the same bubble, and the second is the probability that the points are ionized in separate bubbles. Then

$$P_{2|1}(r) = \frac{1}{\langle V_b\rangle}\int dRP(R)V_b(R)f\left(\frac{r}{R}\right), \quad (21)$$

where $f(r/R)$ is the probability of ionization at $\mathbf{r}_2$ given $\mathbf{r}_1$ in an ionization bubble of radius R, with $r = |\mathbf{r}_1 - \mathbf{r}_2|$.

Suppose the point $\mathbf{r}_1$ is in an ionized bubble of radius R at a distance $r_0 < R$ from the center, and $\mathbf{r}_2$ is separated from $\mathbf{r}_1$ by r. If we consider two spheres with radii R and r, with their centers a distance r_0 apart, then we can define $A(R, r, r_0)$ as the area on the sphere with radius r that is in the interior of the sphere with radius R. The probability that a random point $\mathbf{r}_1$ inside a bubble of radius R is a distance r_0 from the center is $P(r_0)dr_0 = (4\pi r_0^2 dr_0)/V_b(R)$. The function $f(r/R)$ is the integral over r_0 from 0 to R of the fractional area $A(R, r, r_0)/(4\pi r^2)$ times $P(r_0)$, which gives

$$f\left(\frac{r}{R}\right) = 1 - \frac{3}{4}\frac{r}{R} + \frac{1}{16}\left(\frac{r}{R}\right)^3, \; r \leq 2R, \tag{22}$$

and $f(r/R) = 0$ for $r > 2R$. Assuming there is not significant overlap between bubbles, this function $f(r/R)$ is the convolution of $V_b W_R(r)$ with itself and its Fourier transform is $V_b W_R^2(k)$ (Wang & Hu 2006):

$$\begin{aligned} f\left(\frac{r}{R}\right) &= \frac{1}{V_b(R)} \int d^3r' V_b^2(R) W_R(\mathbf{r} - \mathbf{r}') W_R(\mathbf{r}') \\ &= V_b(R) \int \frac{d^3k}{(2\pi)^3} W_R^2(k) e^{-i\mathbf{k}\cdot\mathbf{r}}. \end{aligned} \tag{23}$$

The overlap between bubbles will be small if $\bar{n}_b \langle V_b \rangle \ll 1$, which corresponds to $x_e \ll 0.63$ by equation (7). This assumption should be valid until near the end of reionization.

Using this expression for $f(r/R)$ with equations (20) and (21), the ionization correlation function is

$$\xi^{1b}_{\delta x \delta x}(r) = (x_e - x_e^2) P_{2|1}(r), \tag{24}$$

$$P_{2|1}(r) = \frac{1}{\langle V_b \rangle} \int dR \; P(R) V_b^2(R) \int \frac{d^3k}{(2\pi)^3} W_R^2(k) e^{-i\mathbf{k}\cdot\mathbf{r}}.$$

We can take the Fourier transforms of $\xi^{1b}_{\delta x \delta x}$ and $\xi^{1b}_{\delta x \delta x} \xi_{\delta\delta}$ to get the 1-bubble terms in the power spectrum

$$P^{1b}_{\delta x \delta x}(k) = \frac{x_e - x_e^2}{\langle V_b \rangle} \int dR \; V_b^2(R) P(R) W_R^2(k), \tag{25}$$

$$P^{1b}_{\delta x \delta \; \delta x \delta}(k) = (x_e - x_e^2) \tilde{P}(k). \tag{26}$$

The first term, equation (25), is associated with the shot noise of the bubbles. In the second term, equation (26), $\tilde{P}(k)$ is the convolution of the matter power spectrum $P(k)$ with the square of the one-bubble averaged window function,

$$\tilde{P}(k) = \langle V_b \rangle \int \frac{d^3k_1}{(2\pi)^3} \langle W_R^2(k) \rangle P(|\mathbf{k} - \mathbf{k}_1|), \tag{27}$$

where the one-bubble window function averaged over the bubble radius distribution is defined by

$$\langle W_R^2(k) \rangle = \frac{1}{\langle V_b \rangle^2} \int dR \; V_b^2(R) P(R) W_R^2(k). \tag{28}$$

As in Wang & Hu (2006), we simplify our calculations by approximating $\tilde{P}(k)$ by interpolating between its small and large k limits:

$$\tilde{P}(k) \approx \frac{P(k) \langle V_b \rangle \langle \sigma_R^2 \rangle}{[(P(k))^2 + (\langle V_b \rangle \langle \sigma_R^2 \rangle)^2]^{1/2}}, \tag{29}$$

where $\langle \sigma_R^2 \rangle$ is the top-hat smoothed density variance averaged over the bubble radius distribution

$$\langle \sigma_R^2 \rangle = \frac{1}{\langle V_b \rangle^2} \int dR \; V_b^2(R) P(R) \sigma_R^2. \tag{30}$$

The total one-bubble contribution to the H II power spectrum is the sum of equations (25) and (26),

$$P^{1b}_{\delta_{\rm HII}}(k) = x_e(1 - x_e) \left[\langle V_b \rangle \langle W_R^2(k) \rangle + \tilde{P}(k) \right]. \tag{31}$$

2.3. *Bubble Radius Distribution*

To evaluate the power spectrum, we need to specify the bubble radius distribution which determines the averaged window functions $\langle W_R(k) \rangle$ and $\langle W_R^2(k) \rangle$. Motivated by the analytic model of Furlanetto et al. (2004) and numerical simulations (Zahn et al. 2007), we assume here a log normal distribution with width $\sigma_{\ln R}$:

$$P(R) = \frac{1}{R} \frac{1}{\sqrt{2\pi\sigma^2_{\ln R}}} e^{-[\ln(R/\bar{R})]^2/2\sigma^2_{\ln R}}. \tag{32}$$

This distribution is shown in Figure 1 for $\sigma_{\ln R} = 0.2$ and $\sigma_{\ln R} = 1.0$.

The one and two bubble terms in the power spectrum possess different weights over this distribution. From equation (16) using a log normal $P(R)$, the two-bubble averaged window function is

$$\begin{aligned} \langle W_R(k) \rangle = &\frac{3e^{-9\sigma^2_{\ln R}/2}}{\sqrt{2\pi}\sigma_{\ln R}} \int_0^\infty d\chi \; \chi^2 e^{-\ln^2 \chi / 2\sigma^2_{\ln R}} \\ &\times \frac{\sin\kappa\chi - \kappa\chi\cos\kappa\chi}{(\kappa\chi)^3} \end{aligned} \tag{33}$$

where $\kappa \equiv k\bar{R}$ and $\chi \equiv R/\bar{R}$. Similarly, for the one-bubble terms, equation (28) becomes

$$\begin{aligned} \langle W_R^2(k) \rangle = &\frac{9e^{-9\sigma^2_{\ln R}}}{\sqrt{2\pi}\sigma_{\ln R}} \int_0^\infty d\chi \; \chi^5 e^{-\ln^2 \chi / 2\sigma^2_{\ln R}} \\ &\times \frac{(\sin\kappa\chi - \kappa\chi\cos\kappa\chi)^2}{(\kappa\chi)^6}. \end{aligned} \tag{34}$$

For a given value of $\sigma_{\ln R}$, each of these averaged window functions depends only on $\kappa = k\bar{R}$ and not on k or $\bar{R}$ separately. Figures 2 and 3 show the window functions for various choices of $\sigma_{\ln R}$, evaluated by numerically integrating the expressions in equations (33) and (34).

It is useful to examine the limiting behavior of these window functions to determine the characteristic scale in the average. Using the fact that $\lim_{k\to 0} W_R(k) = 1$, we see from equation (16) that the two-bubble window function $\langle W_R \rangle$ also approaches unity in the limit of small k. In the oscillatory high k regime, the integration will sharply suppress contributions. Thus the weight in the distribution simply reflects the average bubble volume and it is useful to define a volume weighted radius R_0

$$\langle V_b \rangle \equiv \frac{4\pi}{3} R_0^3, \tag{35}$$

which is larger than $\bar{R}$ (see Figure 1)

$$R_0 = e^{3\sigma^2_{\ln R}/2} \bar{R}. \tag{36}$$

The $k \to 0$ limit of equation (28) for the one-bubble window function is

$$\lim_{k\to 0} \langle W_R^2(k) \rangle = \frac{\langle V_b^2 \rangle}{\langle V_b \rangle^2} = e^{9\sigma^2_{\ln R}}, \tag{37}$$

where the second equality holds for the case where $P(R)$ is the log normal distribution. For large k, $W_R^2(k) \approx$

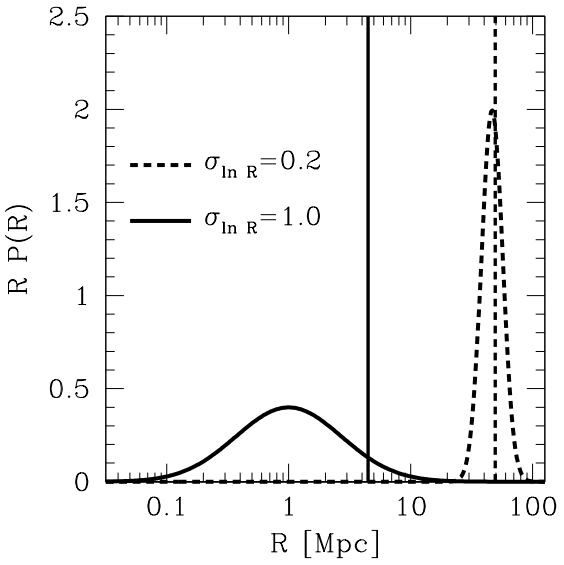

FIG. 1.— H II bubble radius distributions for $\sigma_{\ln R} = 0.2$ (*dashed*) and $\sigma_{\ln R} = 1.0$ (*solid*) with the same effective radius, $R_{\rm eff} = 55$ Mpc. The vertical lines show the location of the volume weighted radius R_0 for each distribution.

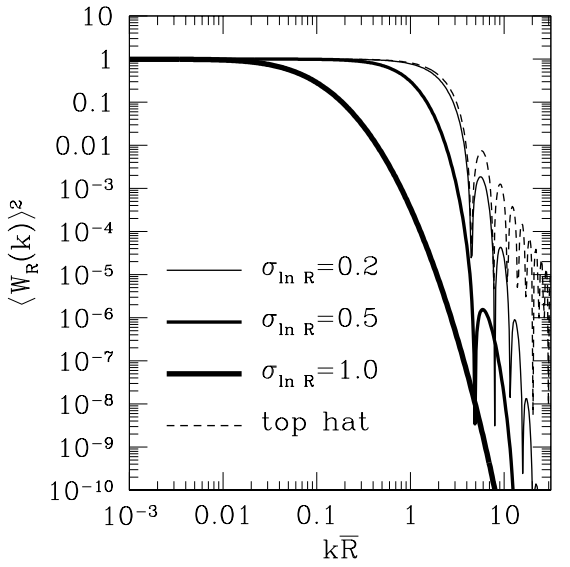

FIG. 2.— Squared two-bubble averaged window functions for log normal bubble radius distributions with widths $\sigma_{\ln R} = 0.2$ (*thin*), 0.5 (*medium*), and 1.0 (*thick*). The square of a top-hat window function is plotted for comparison (*dashed*).

$9(kR)^{-4}\cos^2(kR)$. Since $\cos^2(kR)$ oscillates rapidly in this limit compared with the variation of $V_b^2 P(R) R^{-4}$, we can replace $(\sin\kappa\chi - \kappa\chi\cos\kappa\chi)^2$ by 1/2 in the integral in equation (34). Then we have

$$\lim_{k\to\infty}\langle W_R^2(k)\rangle \approx \frac{9e^{-9\sigma_{\ln R}^2}}{2\sqrt{2\pi}\sigma_{\ln R}\kappa^4}\int d\chi\ \chi e^{-\ln^2\chi/2\sigma_{\ln R}^2} = \frac{9}{2}e^{-7\sigma_{\ln R}^2}(k\bar{R})^{-4}. \quad (38)$$

To estimate the characteristic scale in the one-bubble terms, we take the value of k where $\langle W_R^2\rangle$ transitions between these two limits. This wavenumber, $k_{\rm eff}$, can be

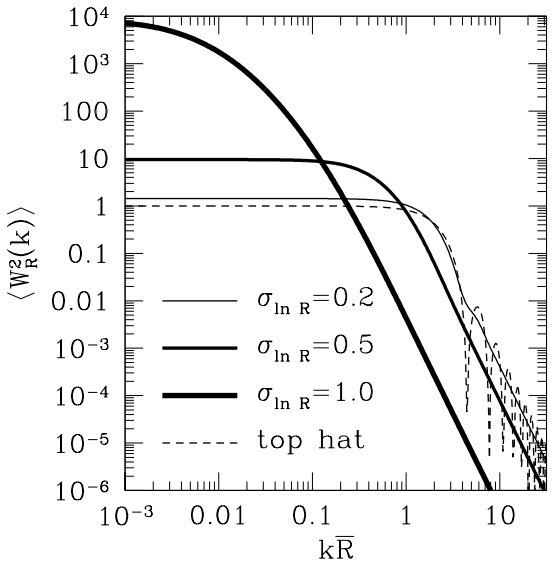

FIG. 3.— Same as Figure 2, but for one-bubble averaged window functions.

estimated by requiring that

$$\lim_{k\to 0}\langle W_R^2(k)\rangle\Big|_{k=k_{\rm eff}} = \lim_{k\to\infty}\langle W_R^2(k)\rangle\Big|_{k=k_{\rm eff}}. \quad (39)$$

Using equations (37) and (38), we find

$$k_{\rm eff} = \left(\frac{9}{2}\right)^{1/4} R_0^{-1} e^{-2.5\sigma_{\ln R}^2}. \quad (40)$$

Therefore, we expect the main contributions to arise from scales

$$R_{\rm eff} \equiv \bar{R}e^{4\sigma_{\ln R}^2} = R_0 e^{2.5\sigma_{\ln R}^2}. \quad (41)$$

Note that the two distributions in Figure 1 have the same $R_{\rm eff}$ even though their $\bar{R}$ differ by a factor of ~ 50. In the $\sigma_{\ln R} \to 0$ limit, $R_{\rm eff} = \bar{R} = R_0$ so all the polarization power comes from bubbles with radii equal to $R_{\rm eff}$. For larger values of $\sigma_{\ln R}$, we find that most of the power is still due to bubbles with $R \sim R_{\rm eff}$.

3. PARAMETERIZATION OF REIONIZATION MODELS

The framework for inhomogeneous reionization described in the previous section requires the specification of three functions of redshift: the ionization fraction $x_e(z)$, the volume weighted bubble radius $R_0(z)$ defined by equation (35), and the width of the log normal radius distribution $\sigma_{\ln R}(z)$. In this section we discuss several parameterizations of these functions that highlight their impact on the B-modes.

We begin by discussing the leading order shot noise term contributing to the B-mode spectrum and how it determines the shape of the spectrum in Section 3.1. We parameterize the range of redshifts for which $0 < x_e < 1$ by z_i and z_f, the redshift at the beginning and end of reionization respectively. In Section 3.2, we explore the impact of various choices for $x_e(z)$ during this epoch, including histories that maximize the B-modes and integral constraints from the total optical depth τ_*. Finally we take two representative forms for $R_0(z)$ in Section 3.3, a constant radius set by $R_{\rm eff}$ the characteristic radius of

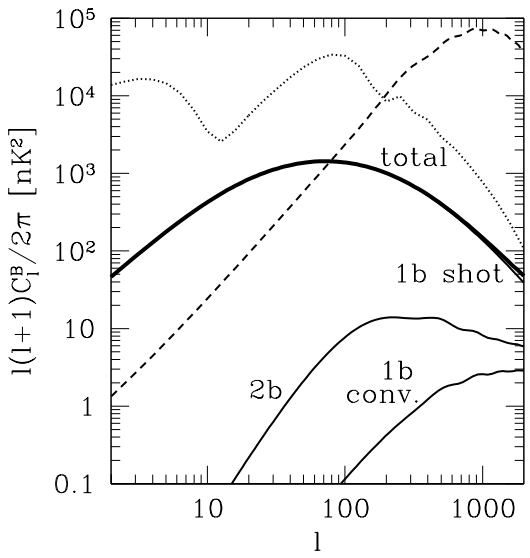

FIG. 4.— An example of a B-mode polarization spectrum from inhomogeneous reionization (*solid, thick*), and the contributions to the spectrum from each component of the H II power spectrum in equation (42) (*thin, solid curves* as labelled): the one-bubble shot noise term, the one-bubble convolution term, and the two-bubble term. The reionization model that produces this polarization (model 19 in Table 2) has a linear ionization history, constant $\bar{n}_b$, $z_f = 6$, $z_i = 18.4$, $\tau_* = 0.12$, $\sigma_{\ln R} = 1.0$, and $R_0(z_f) = 50$ Mpc ($R_{\rm eff}(z_f) = 609$ Mpc). The lensing B-modes for the assumed cosmology (*dashed*) and the gravitational wave B-modes with tensor-to-scalar ratio $r = 0.5$ (*dotted*) are plotted for comparison.

the bubbles for the dominant shot noise term, and a constant number density of bubbles $\bar{n}_b$ which grow in radius. For simplicity we take a constant $\sigma_{\ln R}$ throughout.

3.1. *Approximate B-mode Spectrum*

Different components of the H II power spectrum can vary greatly in how much they contribute to $\mathcal{C}_\ell^B$ at a particular scale. We study the relative contributions by separating the power spectrum into the one-bubble shot noise term, the one-bubble convolution term, and the two-bubble term

$$P_{\delta_{\rm HII}} = P^{1b}_{\delta x \delta x} + P^{1b}_{\delta x \delta\ \delta x \delta} + P^{2b}_{\delta_{\rm HII}} \qquad (42)$$

and integrating equation (1) replacing $P_{\delta_{\rm HII}}$ by each of these three terms. Figure 4 shows these contributions to the total B-mode spectrum for a particular reionization model. The lensing and gravitational wave B-modes plotted in Figure 4 show that B-modes from inhomogeneous reionization would be an important contaminant for gravitational waves if they have a large amplitude at $\ell \lesssim 100$, so we sometimes focus on the B-mode amplitude at $\ell \sim 100$.

For all values of model parameters we consider, the contribution to $\mathcal{C}_\ell^B$ from the convolution term, $P^{1b}_{\delta x \delta\ \delta x \delta}$, is less than the contributions from the other two terms.

For some choices of parameters, the contribution from $P^{2b}_{\delta_{\rm HII}}$ is dominant over a range of ℓ values. In these cases, however, the B-mode amplitude is never larger than a few tens of nK^2. The amplitude of the two-bubble contribution is limited by the fact that $\langle W_R^2(k)\rangle$ is never greater than 1, and because $P(k)$ decreases with redshift.

All of the models with large B-modes ($\mathcal{C}_\ell^B \gtrsim 100$ nK^2) at $\ell \sim 100$ are dominated by the one-bubble shot noise term in the H II power spectrum, $P^{1b}_{\delta x \delta x}$ (e.g., the model in Figure 4). Note that this is the only term in the H II power spectrum that is independent of the matter power spectrum.

Since the shot noise term dominates the polarization spectrum, we can understand much of the dependence on reionization parameters by approximating the B-mode spectrum by its shot noise contribution. For these models $\mathcal{C}_\ell^B$ is well described as a single, wide peak. We will often give our results by stating the multipole of this peak, $\ell_{\rm peak}$, and its amplitude $(\mathcal{C}_\ell^B)_{\rm peak}$.

The scale $\ell_{\rm peak}$ is primarily determined by the bend in the averaged one-bubble window function $\langle W_R^2\rangle$, which is set by $R_{\rm eff}$ as described in Section 2.3. More specifically $\ell_{\rm peak} = k_{\rm eff}/D_A$ and since the angular distance varies slowly during reionization, the shot noise-dominated B-mode power should peak at

$$\ell_{\rm peak} \propto R_{\rm eff}^{-1} \qquad (43)$$

with power law behavior as $\mathcal{C}_\ell^B \sim \ell^2$ on large scales and $\mathcal{C}_\ell^B \sim \ell^{-2}$ on small scales. Because of the crucial role $R_{\rm eff}$ plays in setting the multipole at which the polarization spectrum peaks, we present our results in terms of $R_{\rm eff}$ rather than R_0.

The amplitude of the peak depends on multiple parameters of the ionization model as we describe in Section 4.

3.2. *Ionization Fraction*

To explore the dependence of the B-modes on $x_e(z)$, we use a variety of types of ionization histories.

We assume that $x_e = 0$ for $z > z_i$ and $x_e = 1$ for $z < z_f$. During the epoch of reionization, we require $0 \le x_e \le 1$. The optical depth places an additional constraint on $x_e(z)$. The optical depth out to redshift z is

$$\tau(z) = \sigma_T n_{p,0} \int_0^z dz' \frac{(1+z')^2}{H(z')} x_e(z'). \qquad (44)$$

We can use the range of observed values for the total optical depth $\tau_* = \tau(z \ge z_i)$ to constrain $x_e(z)$ through equation (44). Note that the epoch of reionization can start no later than $z_i \approx 12.4$ if $\tau_* = 0.12$, or $z_i \approx 7.7$ if $\tau_* = 0.06$.

The polarization signal we are concerned with only comes from redshifts $z_f < z < z_i$, so we will define the optical depth from the epoch of reionization $\tau_{\rm rei} \equiv \tau_* - \tau(z_f)$, where $\tau(z_f)$ depends only on z_f and cosmological parameters that we hold fixed.

To derive approximate expressions in the following sections, we will often assume that the universe is matter dominated so that $H(z) \approx H_0\sqrt{\Omega_{\rm m}}(1+z)^{3/2}$. This is a good approximation during the epoch of reionization.

3.2.1. *Constant Ionization Fraction*

The simplest model is a constant value of x_e throughout the epoch of reionization. For a fixed value of τ_*, the ionization fraction in this model is

$$x_e = \frac{3\tau_{\rm rei}}{2\tau_0}\left[(1+z_i)^{3/2} - (1+z_f)^{3/2}\right]^{-1}, \qquad (45)$$

where $\tau_0 = \sigma_T n_{p,0}/(\sqrt{\Omega_{\rm m}} H_0)$.

Although a model with constant x_e is far from being a realistic model of reionization, it is a useful simplifying assumption for finding the approximate dependence of $\mathcal{C}_\ell^B$ on other parameters of the model.

3.2.2. *Linear Ionization Fraction*

As a more realistic model of reionization we consider an ionization fraction that decreases linearly with redshift,

$$x_e(z) = 1 - \frac{z - z_f}{z_i - z_f}. \quad (46)$$

For a fixed value of τ_*, the redshifts z_i and z_f cannot be varied independently since they are related through equation (44). In our linear ionization histories, we fix τ_* and z_f and determine the required value for z_i. The upper panel of Figure 5 shows a linear $x_e(z)$ for a model with $\tau_* = 0.12$ and $z_f = 6$.

3.2.3. *Maximal B-Mode Ionization History*

If we approximate the H II power spectrum by the shot noise term $P^{1b}_{\delta x \delta x}$, and use the fact that $D_A(z)$, $Q_{\rm rms}(z)$, and $\tau(z)$ vary slowly with redshift during reionization to pull these factors out of the integral in equation (1), then the dependence of the B-mode amplitude on the ionization history is approximately

$$\mathcal{C}_\ell^B \sim \int_{z_f}^{z_i} dz (1+z)^{5/2} x_e(z)[1 - x_e(z)]. \quad (47)$$

We can use variational calculus to determine what form of $x_e(z)$ maximizes this integral, giving the largest B-mode amplitude in this approximation.

Fixing the total optical depth τ_* (and therefore $\tau_{\rm rei} = \tau_* - \tau(z_f)$) gives an integral constraint on $x_e(z)$,

$$\frac{\tau_{\rm rei}}{\tau_0} = \int_{z_f}^{z_i} dz (1+z)^{1/2} x_e(z), \quad (48)$$

so we can define

$$f(z, x_e, x_e') = (1+z)^{5/2} x_e(1 - x_e) + \lambda (1+z)^{1/2} x_e, \quad (49)$$

where $x_e' = dx_e/dz$ and λ is a Lagrange multiplier. Since this function is independent of x_e', the Euler-Lagrange equation is just $\partial f/\partial x_e = 0$. Solving for $x_e(z)$ gives

$$x_e(z) = \frac{1}{2} + \frac{\lambda}{2}(1+z)^{-2}. \quad (50)$$

The ionization fraction given by this equation approaches 1/2 at high redshift. For lower values of z, x_e must stay between by 0 and 1. These limits are satisfied for redshifts $z \geq |\lambda|^{1/2} - 1$. If z_f satisfies this inequality, then $x_e(z)$ as given by equation (50) is between 0 and 1 during the entire epoch of reionization. If not, then for redshifts $z_f < z < |\lambda|^{1/2} - 1$, x_e is saturated at either 0 or 1 depending on the sign of λ.

The values we assume for τ_*, z_i, and z_f determine the sign of λ. If $\lambda > 0$, then $x_e > 1/2$ for all z, so $\tau_{\rm rei}/\tau_0$ must be greater than it would be with constant $x_e = 1/2$. If $\lambda < 0$ the ionization fraction is always less than 1/2 and $\tau_{\rm rei}/\tau_0$ is less than the constant $x_e = 1/2$ value. We can define an optical depth τ_λ corresponding to the case $x_e(z) = 1/2$

$$\frac{\tau_\lambda(z_i, z_f)}{\tau_0} = \frac{1}{3}\left[(1+z_i)^{3/2} - (1+z_f)^{3/2}\right], \quad (51)$$

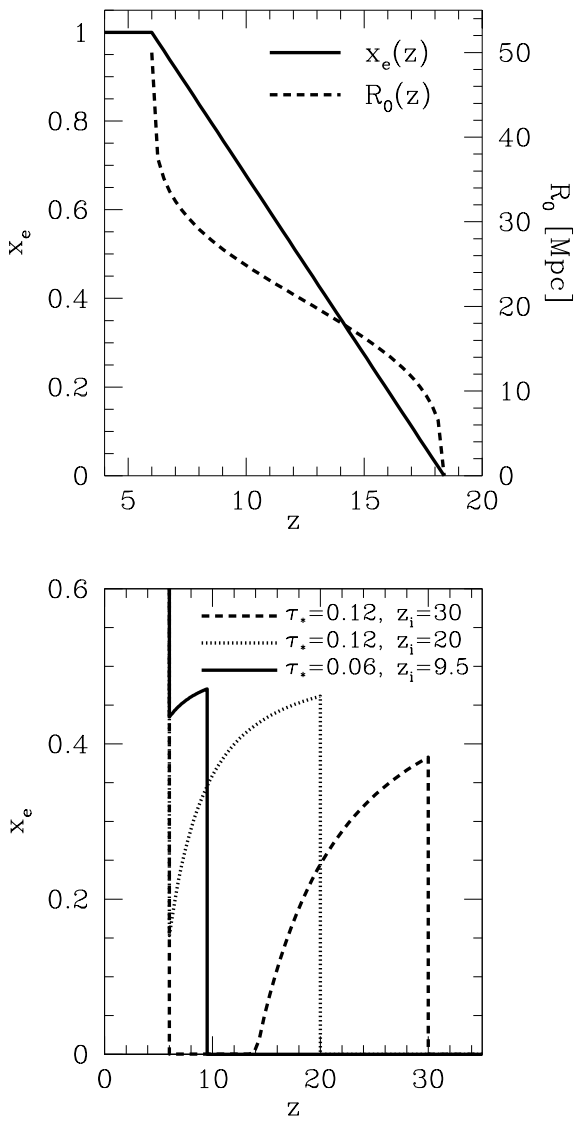

FIG. 5.— *Upper panel*: Ionization history and characteristic bubble radius for a linear $x_e(z)$ model with $z_f = 6$, $z_i = 18.4$, $\tau_* = 0.12$, and fixed $\bar{n}_b$ (model 19 in Table 2). *Lower panel*: Ionization histories for three maximal-$x_e(z)$ models (models 8-10 in Table 1). The ionization fraction in all three models increases to 1 for $z \leq 6$.

so that λ in equation (50) must have the same sign as $\tau_{\rm rei} - \tau_\lambda$. For $z_f = 6$ and $z_i = 20$, $\tau_\lambda \approx 0.1$; for $z_f = 6$ and $z_i = 30$, $\tau_\lambda \approx 0.2$.

After determining the sign of λ for particular choices of τ_*, z_i, and z_f, the magnitude of λ is fixed by the optical depth constraint, equation (48), using equation (50) for $x_e(z)$ over the appropriate range of redshifts. The resulting ionization histories for three combinations of τ_* and z_i are plotted in the lower panel of Figure 5.

The maximal-polarization ionization histories are even less realistic than those described in the previous sections, since they have a significant ionization fraction ($x_e \lesssim 1/2$) at high redshift, and x_e can be small or even zero near the end of reionization, if $\lambda < 0$. These models are useful, however, because the B-mode amplitudes associated with them provide an upper limit that B-modes

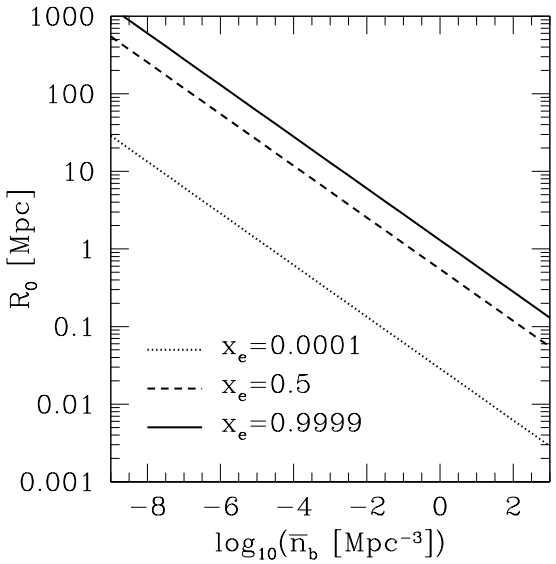

FIG. 6.— Volume averaged bubble radius R_0 versus bubble comoving number density for ionization fractions $x_e = 0.0001$, 0.5, and 0.9999. Fixed R_0 models correspond to horizontal trajectories between $x_e \approx 0$ and $x_e \approx 1$, and fixed $\bar{n}_b$ models are vertical trajectories in this plot.

from more realistic reionization scenarios must lie below.

Note that due to the approximations leading to equation (47), the actual ionization history that maximizes the B-mode amplitude will differ slightly from the one derived here in equation (50). The results of Monte Carlo models that vary $x_e(z)$ in each redshift bin suggest that the true maximal $x_e(z)$ is not very different from the approximation used here. The B-mode amplitude of the true maximal-x_e model is likely only a few percent larger than the model of equation (50), and even if the amplitude were much larger it would be only for a finely tuned (and unrealistic) ionization history missed in the Monte Carlo search. It is reasonable, therefore, to take the B polarization produced by models of the approximate form derived here as an effective upper limit on the amplitude that can be reached by varying $x_e(z)$ with τ_* and all other reionization parameters held fixed.

3.3. *Bubble Radius*

We consider two ways of modelling the evolution of the bubble size distribution. In one, we assume a fixed comoving bubble number density $\bar{n}_b$ throughout reionization, so that the global ionization fraction increases only due to bubble growth. The normalization of the bubble radius evolution is set by specifying the comoving characteristic bubble radius at the end of reionization, $R_{\mathrm{eff},f}$. The evolution of R_{eff} in a fixed-$\bar{n}_b$ model with a linear ionization history is shown in the upper panel of Figure 5.

The second type of model has a fixed distribution of radii, so R_{eff} is independent of z. In this model, the ionization fraction increases as more ionizing sources collapse and turn on, while the size of individual bubbles remains constant.

In the radius-number density plane, these models can be thought of as trajectories along a horizontal path from $x_e = 0$ to $x_e = 1$ for fixed R_{eff}, and vertical trajectories for fixed $\bar{n}_b$ (Figure 6). We assume throughout that $\sigma_{\ln R}$ does not vary with redshift, so the evolution of R_0 and $\bar{R}$ is the same as that of R_{eff} up to a $\sigma_{\ln R}$-dependent normalization.

TABLE 1
MULTIPOLES AND AMPLITUDES OF B POLARIZATION SPECTRA PEAKS FOR REIONIZATION MODELS WITH DIFFERENT TYPES OF IONIZATION HISTORIES: CONSTANT (C), LINEAR (L), AND FOR MAXIMAL B-MODES (M).

Model	τ_*	z_i	z_f	$x_e(z)$	fixed $R_{\mathrm{eff}}/\bar{n}_b$	$\sigma_{\ln R}$	$R_{\mathrm{eff},f}$ [Mpc]	ℓ_{peak}	$(\mathcal{C}_\ell^B)_{\mathrm{peak}}$ [nK^2]
1	0.12	20	6	C	both	1.0	609	28	8836
2	0.12	30	6	C	both	1.0	609	30	23050
3	0.12	40	6	C	both	1.0	609	32	45049
4	0.06	9.3	6	L	R_{eff}	1.0	609	24	422
5	0.12	18.4	6	L	R_{eff}	1.0	609	27	4325
6	0.12	16.6	8	L	R_{eff}	1.0	609	27	2944
7	0.12	14.8	10	L	R_{eff}	1.0	609	27	1600
8	0.06	9.5	6	M	R_{eff}	1.0	609	24	692
9	0.12	20	6	M	R_{eff}	1.0	609	28	8989
10	0.12	30	6	M	R_{eff}	1.0	609	31	27611
11	0.12	40	6	M	R_{eff}	1.0	609	32	62667

4. *B*-MODE PARAMETER DEPENDENCE

In the previous section, we parameterized the ionization history $x_e(z)$ and the effective bubble size $R_{\mathrm{eff}}(z)$ under several simple schemes that were designed to bring out the critical properties of a reionization model for the B-mode spectrum. In this section we explore these properties and provide scaling relations for the impact of reionization parameters on B-modes.

4.1. *Ionization History*

Table 1 gives the B-mode peak multipoles and amplitudes for reionization models with the different ionization histories described in Section 3.2. For fixed values of τ_*, z_i, z_f, $\sigma_{\ln R}$, and $R_{\mathrm{eff}}(z)$, we find that changing the shape of the ionization history has only a mild effect on the B-mode spectrum compared with the effects of the other reionization parameters.

For example, compare models 1, 5, and 9, which all have $\tau_* = 0.12$, $z_i \approx 20$, $z_f = 6$, $\sigma_{\ln R} = 1.0$, and $R_{\mathrm{eff}} = 609$ comoving Mpc ($R_0 = 50$ Mpc). All of these models produce B-modes that peak at $\ell_{\mathrm{peak}} \approx 28$. There is about a factor of two difference between the largest peak amplitude of these four models (model 9, maximal $x_e(z)$ with $(\mathcal{C}_\ell^B)_{\mathrm{peak}} = 8989$ nK^2), and the smallest (model 5, linear $x_e(z)$ with $(\mathcal{C}_\ell^B)_{\mathrm{peak}} = 4325$ nK^2).

The results are similar if we adopt different values for the reionization parameters other than $x_e(z)$. For example, models 4 and 8, both with $\tau_* = 0.06$, $z_i \approx 9.5$, $z_f = 6$, and the same $R_{\mathrm{eff}}(z)$, have the same peak multipole, and their B-mode amplitudes differ by less than a factor of two between the maximal and linear $x_e(z)$ models.

Looking at the entire set of models presented in Table 1, there is a wide variety of B-mode peak scales and amplitudes. However, the largest differences occur between models with different choices of τ_*, z_i, z_f, or $R_{\mathrm{eff}}(z)$.

TABLE 2
MULTIPOLES AND AMPLITUDES OF B POLARIZATION SPECTRA PEAKS FOR REIONIZATION MODELS VARYING $R_{\rm eff}$ AND $\sigma_{\ln R}$.

Model	τ_*	z_i	z_f	$x_e(z)$	fixed $R_{\rm eff}/\bar{n}_b$	$\sigma_{\ln R}$	$R_{{\rm eff},f}$ [Mpc]	$\ell_{\rm peak}$	$(\mathcal{C}_\ell^B)_{\rm peak}$ [nK^2]
12	0.12	30	6	C	both	1.0	50	400	1928
13	0.12	30	6	C	both	0.5	50	407	4249
14	0.12	30	6	C	both	0.2	50	450	6276
15	0.12	30	6	C	both	1.0	500	37	19057
16	0.12	30	6	C	both	0.5	500	40	42711
17	0.12	30	6	C	both	0.2	500	45	63289
18	0.06	9.3	6	L	$\bar{n}_b$	1.0	609	59	161
19	0.12	18.4	6	L	$\bar{n}_b$	1.0	609	72	1544
20	0.12	16.6	8	L	$\bar{n}_b$	1.0	609	69	1092
21	0.12	14.8	10	L	$\bar{n}_b$	1.0	609	66	619

4.2. *H II Bubble Size Distribution*

The reionization models in Table 2 and Figure 7 show the dependence of $\ell_{\rm peak}$ and $(\mathcal{C}_\ell^B)_{\rm peak}$ on H II bubble size. Larger values of $R_{\rm eff}$ lead to a smaller multipole for the B-mode peak (see equation (43))

$$\ell_{\rm peak} \approx 100 \left(\frac{200\ {\rm Mpc}}{R_{\rm eff}}\right). \qquad (52)$$

We can see the relation between $R_{\rm eff}$ and $\ell_{\rm peak}$ in the models in Table 2. For example, models 12-14 have different values of $\sigma_{\ln R}$ but the same $R_{\rm eff}$, and $\ell_{\rm peak}$ is the same to within about 10%. As $R_{\rm eff}$ increases, not only does $\ell_{\rm peak}$ decrease but also the amplitude of the peak increases. For a fixed $\sigma_{\ln R}$ it scales as $(\mathcal{C}_\ell^B)_{\rm peak} \propto R_{\rm eff}$.

The dependence of the amplitude on the width $\sigma_{\ln R}$ at fixed $R_{\rm eff}$ is much weaker. Note that the B-mode peak amplitude for the dominant shot noise contributions can be approximated as

$$(\mathcal{C}_\ell^B)_{\rm peak} \sim R_0^3 \langle W_R^2(k_{\rm eff})\rangle \sim e^{-7.5\sigma_{\ln R}^2} \langle W_R^2(k_{\rm eff})\rangle\,, \quad (53)$$

for fixed $R_{\rm eff}$. Defining

$$\kappa_{\rm eff} \equiv k_{\rm eff}\bar{R} = \left(\frac{9}{2}\right)^{1/4} e^{-4\sigma_{\ln R}^2}, \qquad (54)$$

equation (34) shows that $\langle W_R^2(k_{\rm eff})\rangle$ is a function of $\sigma_{\ln R}$ only. Evaluating the integral in equation (34), we find that $e^{-7.5\sigma_{\ln R}^2}\langle W_R^2(k_{\rm eff})\rangle$ is maximized as $\sigma_{\ln R} \to 0$ and decreases as $\sigma_{\ln R}$ increases, suggesting that $(\mathcal{C}_\ell^B)_{\rm peak}$ has the same behavior. This happens because the spectrum is more sharply peaked as $\sigma_{\ln R} \to 0$, which follows from the fact that the window functions $\langle W_R^2(k)\rangle$ for smaller values of $\sigma_{\ln R}$ bend more sharply at $k = k_{\rm eff}$ (see Figure 3). This maximum amplitude is estimated to be approximately 3 times larger than for the same model with $\sigma_{\ln R} = 1$ (see Figure 7).

The models in Table 2 also show this trend with $\sigma_{\ln R}$, and more generally for the range of $\sigma_{\ln R}$ explored in our models, the scaling of the peak amplitude with $\sigma_{\ln R}$ at fixed $\ell_{\rm peak}$ shows good quantitative agreement with equation (53).

Models 12-17 and the approximate scaling of $\ell_{\rm peak}$ and $(\mathcal{C}_\ell^B)_{\rm peak}$ with $R_{\rm eff}$ assume constant $R_{\rm eff}$ throughout reionization, but the same general results apply when $R_{\rm eff}$ is changing. The only difference is that the constant radius must be replaced in the scaling relations by an effective radius averaged over the duration of reionization,

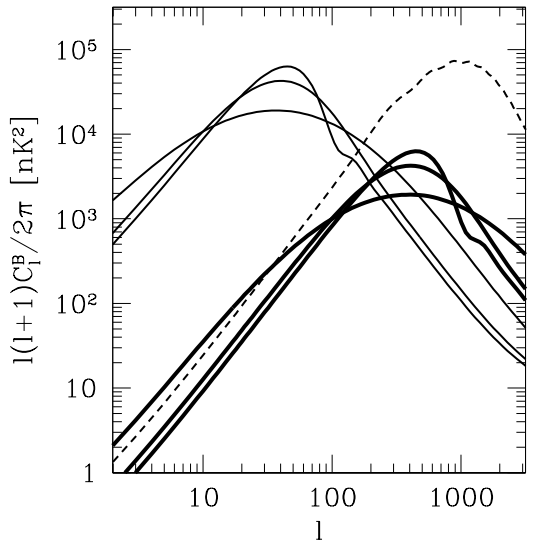

FIG. 7.— B-mode polarization from inhomogeneous reionization with various parameters for the bubble size distribution (models 12-17 in Table 2). The three curves with $\ell_{\rm peak} \approx 40$ have $R_{\rm eff} = 500$ Mpc (*solid, thin*), and the three with $\ell_{\rm peak} \approx 400$ have $R_{\rm eff} = 50$ Mpc (*solid, thick*), with fixed $R_{\rm eff}$ during reionization. For each value of $R_{\rm eff}$, from the widest spectrum to the narrowest (lowest to highest peak amplitude), $\sigma_{\ln R} = 1$, 0.5, and 0.2 respectively. For all models, the other parameters are $z_i = 30$, $z_f = 6$, and $\tau_* = 0.12$, with a constant ionization fraction during reionization. The dashed curve shows the predicted B polarization from gravitational lensing of E-modes for our assumed cosmological parameters.

weighted by the redshift-dependent factors that appear in the integral for $\mathcal{C}_\ell^B$. Models with fixed-$\bar{n}_b$ in which the radius grows with time are shown in Table 1 (18-21). The $\ell_{\rm peak}$ values for these models indicate that the redshift-averaged radius for these models is $R_{\rm eff} \sim 300$ Mpc ($R_0 \sim 25$ Mpc).

For a slowly varying $R_{\rm eff}$ and x_e, equation (47) implies that half the shot noise contributions come from $0.8 < (1+z)/(1+z_i) < 1$. The B-mode amplitude roughly follows the scalings of the constant $R_{\rm eff}$ model with $R_{\rm eff}$ evaluated at $z = 0.8(1+z_i) - 1$. This expectation is borne out by models 5 and 19 (see upper panel of Figure 5). More generally for models where $R_{\rm eff}$ decreases with redshift from its final value, as in the fixed-$\bar{n}_b$ models, the B-mode peak decreases in amplitude and shifts to higher multipoles.

4.3. *Reionization Redshift and Total Optical Depth*

Table 3 and Figure 8 show models with different values of z_i, z_f, and τ_*. The scalings with these parameters can be understood from the shot noise approximation in equation (47)

$$\mathcal{C}_\ell^B \propto x_e(1-x_e)[(1+z_i)^{7/2} - (1+z_f)^{7/2}] \qquad (55)$$

if x_e is constant during reionization, with $x_e(\tau_{\rm rei}, z_i, z_f)$ given by equation (45). Note that the available optical depth during the inhomogeneous period $\tau_{\rm rei}$ sets the ionization fraction, not the total optical depth τ_*, and $\tau_{\rm rei}$ is about a factor of 4 larger when $\tau_* = 0.12$ than when $\tau_* = 0.06$ if $z_f = 6$. The ionization fraction between these two cases then also differ by roughly a factor of 4, but this translates into a somewhat smaller difference in

TABLE 3
MULTIPOLES AND AMPLITUDES OF B POLARIZATION SPECTRA PEAKS FOR REIONIZATION MODELS VARYING z_i, z_f, AND τ_*.

Model	τ_*	z_i	z_f	$x_e(z)$	fixed $R_{\rm eff}/\bar{n}_b$	$\sigma_{\ln R}$	$R_{{\rm eff},f}$ [Mpc]	$\ell_{\rm peak}$	$(\mathcal{C}_\ell^B)_{\rm peak}$ [nK^2]
22	0.12	15	6	C	both	0.5	93	194	962
23	0.12	20	6	C	both	0.5	93	204	2853
24	0.12	30	6	C	both	0.5	93	217	7872
25	0.12	40	6	C	both	0.5	93	226	15154
26	0.12	50	6	C	both	0.5	93	232	25108
27	0.12	30	8	C	both	0.5	93	218	6272
28	0.12	30	10	C	both	0.5	93	218	4025
29	0.06	15	6	C	both	0.5	93	194	614
30	0.06	50	6	C	both	0.5	93	232	6792

the B-mode amplitudes since $\mathcal{C}_\ell^B$ depends on $x_e(1-x_e)$ and not simply on x_e alone.

The models in Table 3 obey this scaling to good approximation. The largest polarization signals are obtained for models with high $z_i \gg z_f$ where $\mathcal{C}_\ell^B \propto (1+z_i)^2$ (model 26, see also Figure 8) and external bounds on this parameter are the most important to limit B-mode contributions (see Section 5). For less extreme cases, the scaling of equation (55) still holds.

Models 27 and 28 in Table 3 show that ending reionization earlier leads to smaller B-modes from inhomogeneous reionization. There are two reasons for this: the epoch of reionization is shorter, which decreases the term in square brackets in equation (55); and increasing z_f makes the available optical depth $\tau_{\rm rei}$ smaller, which gives a smaller value for x_e. (Note that this second effect could instead act to increase the size of the B polarization if $x_e > 0.5$.) One can check that equation (55) provides a good description of the scaling of B-mode amplitudes with z_f to within a few percent accuracy.

Current observational bounds on the total optical depth to reionization allow for a range of values of τ_* that can have a significant effect on the amplitude of the B-mode spectrum. Comparing models 26 and 30 in Table 3, we see that increasing τ_* by a factor of 2 makes the amplitude larger by a factor of about 3.7. For the shorter epoch of reionization in models 22 and 29, a factor of 2 increase in τ_* amplifies the polarization by a factor of 1.6. Again, these results are well described by equation (55) with x_e determined by τ_*.

In summary, the B-mode amplitude is maximized by making the effective bubble radius $R_{\rm eff}$ match the multipole of interest, making the duration of the epoch of reionization as long as possible, and taking the total optical depth to be as large as possible. Narrow distributions generate the most signal but the dependence is weak out to $\sigma_{\ln R} \lesssim 1$.

5. BOUNDS ON REIONIZATION PARAMETERS

From the previous sections we conclude that the parameters that have the greatest effect on the B-mode signal from inhomogeneous reionization are $R_{\rm eff}$ and z_i. Other parameters can affect the amplitude, but the degree to which they can do so is limited either on theoretical ($x_e(z)$, $\sigma_{\ln R}$) or observational grounds (τ_*, z_f).

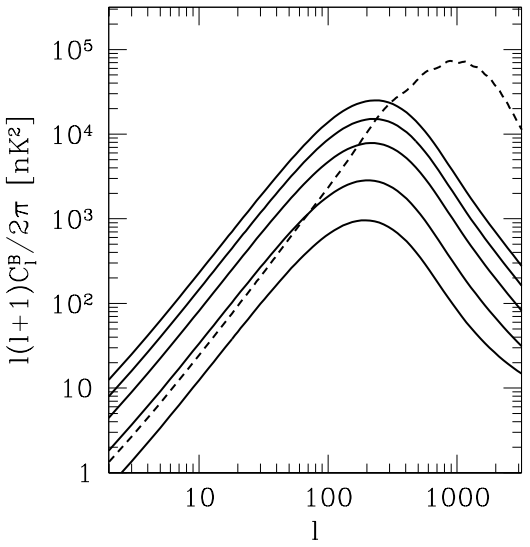

FIG. 8.— B-mode polarization spectra from inhomogeneous reionization, varying the duration of reionization as in models 22-26 in Table 3 (*solid curves*). From top to bottom, the epoch of reionization begins at $z_i = 50$, 40, 30, 20, and 15. For all models, the other parameters are $z_f = 6$, $\tau_* = 0.12$, $\sigma_{\ln R} = 0.5$, and $R_{\rm eff} = 93$ Mpc ($R_0 = 50$ Mpc). The models have constant x_e and $R_{\rm eff}$ during reionization. The dashed curve shows the predicted B-modes from lensing.

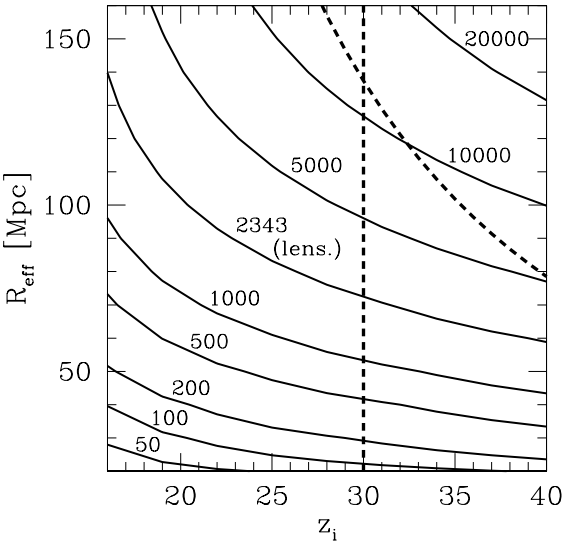

FIG. 9.— Contours of $\mathcal{C}_\ell^B$ at $\ell = 100$ in the $z_i - R_{\rm eff}$ plane. Other reionization parameters are set to $z_f = 6$, $\tau_* = 0.12$, and $\sigma_{\ln R} = 0.2$, and both x_e and $R_{\rm eff}$ are constant during reionization in these models. The units of the labeled contours are nK^2. The contour at 2343 nK^2 marks the power in the lensing B-modes at $\ell = 100$. The dashed curve in the upper right corner shows the comoving radius of a bubble at redshift z_i such that the optical depth from that single bubble along a line of sight passing through the center of the bubble would be equal to the total optical depth, $\tau_* = 0.12$. The vertical dashed line is at the approximate upper limit on z_i from the observed shape of the E-mode reionization peak.

Figure 9 shows contours of $\mathcal{C}_\ell^B$ at $\ell = 100$ in the $z_i - R_{\rm eff}$ plane, with $z_f = 6$ and $\tau_* = 0.12$ chosen to maximize the amplitude. We take $\sigma_{\ln R} = 0.2$ since the amplitude at the peak is maximized at small values of $\sigma_{\ln R}$. As Figure 7 shows, the amplitude on the tails of the spectrum may be higher for larger values of $\sigma_{\ln R}$, but the difference is no more than a factor of a few.

The B-mode amplitude continues to grow as one increases $R_{\rm eff}$ or z_i, so the maximal contributions are determined by observational or theoretical constraints on these quantities.

5.1. *Observational Constraints*

The starting redshift of reionization is limited by the shape and amplitude of the E-mode peak detected in WMAP (Page et al. 2006). The E-mode peak scale is determined by the horizon scale during reionization and an early period of reionization shifts the peak to higher multipoles than observed. For example, consider a model with fixed optical depth $\tau_* = 0.09$ and constant ionization fraction out to $z_i = 30$. In this model, the suppression of power at $\ell = 3$, where the weight of the detection lies, is a factor of 2 larger than in an instantaneous reionization model with $\tau_* = 0.06$, while the enhancement of power at $\ell = 10$ is a factor of 4 larger than in a model with $\tau_* = 0.12$. This is consistent with the findings of Spergel et al. (2006) for constant x_e models out to $z_i = 25$ and implies that $z_i < 30$ at approximately the 2σ level. We show this bound as the vertical dashed line in Figure 9.

With this bound, models that have B-mode power in excess of the lensing signal at $\ell = 100$ have $R_{\rm eff} \gtrsim 70$ Mpc. Bubbles with large radii at high redshift also contain a large optical depth. The optical depth from a fully ionized bubble at redshift z with radius R along a line of sight that passes through the center of the bubble is

$$\tau_b = \sigma_T n_{p,0} (1+z)^2 2R. \tag{56}$$

This single bubble optical depth can exceed the total τ_* if such bubbles have sufficiently low number densities. Despite being rare, they still produce an observable effect on the temperature power spectrum. In the direction of such a bubble, the temperature power spectrum will be suppressed by an additional factor of $e^{-2\tau_b}$. These bubbles would produce a power spectrum of the acoustic peaks which varied from field to field and experiment to experiment. No such effect has been seen and the differences between measurements can be attributed to the $\sim$ 5-10% calibration errors.

Such an effect is also limited by the field-to-field variance of the WMAP power spectrum. Hansen et al. (2004) found no evidence for excess variance beyond the 10% sample variance of the amplitude of the first peak when measured in different 19°-radius patches on the sky.

As a conservative limit, we require that the optical depth from a single bubble should be smaller than the total optical depth to reionization $\tau_* = 0.12$ or a 20% variation in the power in the acoustic peaks on and off of a bubble. For the radius, this constraint becomes

$$R \lesssim 140 \text{ Mpc} \left(\frac{\tau_b}{0.12}\right) \left(\frac{1+z}{31}\right)^{-2}. \tag{57}$$

Since the typical size of a bubble that contributes to the B polarization from inhomogeneous reionization is $R_{\rm eff}$, we apply this constraint to the effective radius. This bound is shown for $\tau_b = 0.12$ as the dashed curve in Figure 9. Combined with equation (52), this also implies a bound on the peak multipole of

$$\ell_{\rm peak} \gtrsim 140 \left(\frac{\tau_b}{0.12}\right)^{-1} \left(\frac{1+z}{31}\right)^{2}. \tag{58}$$

Therefore even if the bound on z_i is relaxed the B-mode contributions at $\ell \sim 100$ would be in the steeply falling white noise tail of the spectrum. Correspondingly the maximal contributions for models in Figure 9 that satisfy this constraint occur for $z_i \lesssim 25$.

This constraint on $R_{\rm eff}$ scales linearly with the optical depth τ_b, so future work similar to that of Hansen et al. (2004) could potentially strengthen this bound. For example, a bound of $\tau_b < 0.06$ would exclude models with B-modes above the lensing signal at $z_i = 30$.

These bounds can potentially be evaded if the width of the distribution $\sigma_{\ln R}$ is so wide that bubbles with $R \sim R_{\rm eff}$ represent such a small fraction of the total that a typical line of sight would never intersect such a bubble. However, if such bubbles are the source of the B-modes, then there would be a large fraction of sky that would be free of this signal. These clean regions of sky could then be used to measure gravitational wave B-modes. To quantify these considerations, we calculate the covering fraction of the sky in bubbles with $R \sim R_{\rm eff}$ as a function of $\sigma_{\ln R}$.

We define the covering fraction as follows. Consider a radius R_p such that p% of the power in the one-bubble shot noise term comes from bubbles with radii $R > R_p$. The median bubble radius that contributes to B-modes is R_{50}, which is within 5-20% of $R_{\rm eff}$ for the range of $\sigma_{\ln R}$ that we consider. We select bubbles with $R \sim R_{\rm eff}$ that contribute half the total power by requiring bubble radii to satisfy $R_{75} < R < R_{25}$. For $\sigma_{\ln R} = 0.2$, $R_{75} = 0.9 R_{\rm eff}$ and $R_{25} = 1.2 R_{\rm eff}$; for $\sigma_{\ln R} = 1$, $R_{75} = 0.8 R_{\rm eff}$ and $R_{25} = 1.6 R_{\rm eff}$.

We also choose a representative range in redshift for the covering fraction. Since most of the polarization signal comes from high-redshift bubbles, we select redshifts $z_i - \Delta z < z < z_i$ at which bubbles contribute half the total B-mode power. In the reionization models we consider, Δz varies between about $0.15(1+z_i)$ and $0.25(1+z_i)$, so we approximate the width in redshift as $\Delta z \approx 0.2(1+z_i)$ (see Section 4.2). Since bubbles with radii between R_{75} and R_{25} contribute half the total power at any given redshift, combining the restrictions on bubble radius and redshift leaves a sample of bubbles that produce a quarter of the B-mode power from inhomogeneous reionization.

In a spherical shell at redshift z_i with width Δz, the number of bubbles per solid angle with radius R is

$$\frac{dN}{dR d\Omega} = P(R) \bar{n}_b D_A^2(z_i) \frac{\Delta z}{H(z_i)}, \tag{59}$$

and the solid angle subtended by a bubble of radius R at distance D_A is $\pi R^2 / D_A^2$. Then the covering fraction of bubbles that meet the criteria for radius and redshift is

$$\begin{aligned} f_{\rm cover} &= \int_{R_{75}}^{R_{25}} dR \frac{dN}{dR d\Omega} \frac{\pi R^2}{D_A^2} \\ &= \frac{3(1+z_i) x_e}{40 H(z_i) R_{\rm eff}} e^{3\sigma_{\ln R}^2/2} \end{aligned} \tag{60}$$

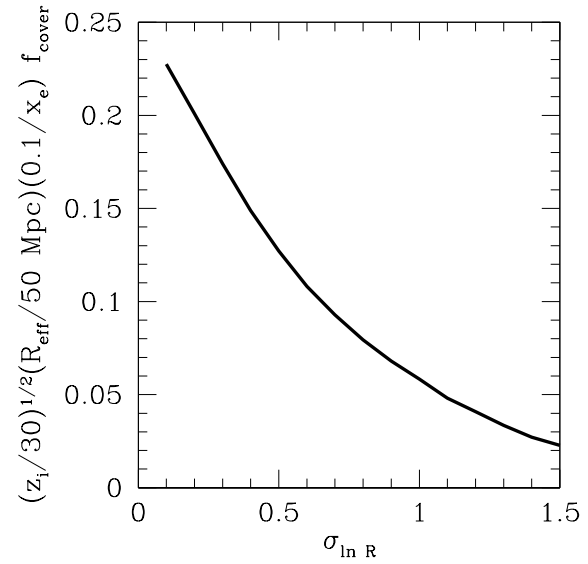

FIG. 10.— The covering fraction of bubbles with radii $R \sim R_{\rm eff}$ at redshifts $z \lesssim z_i$ that are responsible for about 1/4 of the total shot noise power. The covering fraction depends on $R_{\rm eff}$, z_i, and x_e as indicated in the axis label.

$$\times \left[\mathrm{erf}\left(\frac{2\sigma_{\ln R}^2 + \ln r_{25}}{\sqrt{2}\sigma_{\ln R}} \right) - \mathrm{erf}\left(\frac{2\sigma_{\ln R}^2 + \ln r_{75}}{\sqrt{2}\sigma_{\ln R}} \right) \right],$$

where we define $r_p \equiv R_p/R_{\rm eff}$ and assume $\Delta z = 0.2(1 + z_i)$ and $x_e \ll 1$. Note that this is likely to be an overestimate as the covering fraction approaches unity since we assume that the bubbles are not overlapping along lines of sight.

The covering fraction for $z_i = 30$, $R_{\rm eff} = 50$ Mpc, and $x_e = 0.1$ is shown in Figure 10. It becomes negligible for distributions with $\sigma_{\ln R} \gtrsim 1$. The covering fraction decreases for larger z_i, larger $R_{\rm eff}$, or smaller x_e.

5.2. *Theoretical Expectations*

Observational constraints still allow models with large B-mode contributions, approaching and in some cases exceeding the gravitational lens contributions (see Figure 9). However they require $R_{\rm eff} \gtrsim 100$ Mpc at $z_i \sim 20$-30. These models are currently disfavored theoretically as plausible reionization scenarios.

Normal population II star formation is unlikely to be sufficient to cause significant ionization above $z \sim 15$ (see Barkana & Loeb 2001, and references therein). One possibility for obtaining substantial ionization at high redshift is a "double reionization" model where a change in the ionizing sources to say metal free population III stars causes non-monotonic behavior in the ionization fraction (Cen 2003; Wyithe & Loeb 2003). Such models were studied extensively following the indications from the first year WMAP data of a high total optical depth.

Recently, Furlanetto & Loeb (2005) have argued that such models are unlikely to cause a non-monotonic behavior. This would rule out models that have significant ionization at high redshifts compensated by a low value of x_e at intermediate redshifts to keep the total optical depth within the observed limits, such as the maximal B-mode ionization histories we consider. However, Furlanetto & Loeb (2005) find that models with extended periods of ionization in which x_e is significant over a wide range of redshifts out to $z_i \lesssim 20$ are not difficult to find. Recall that such models would produce B-modes that are within a factor of a few of maximal at a given z_i. However given the low σ_8 currently indicated by WMAP (Spergel et al. 2006), extended reionization at high redshift becomes even more difficult to achieve (Alvarez et al. 2006). Recent simulations have nonetheless found that substantial ionization at $z = 15$-20 is still possible with small-mass sources (Iliev et al. 2006).

Even for $z_i \lesssim 20$ substantial B-modes are possible but only if the effective bubble radius $R_{\rm eff} \gtrsim 100$ Mpc. The clustering of sources could create H II regions with comoving radii of 10-30 Mpc near the end of reionization, larger than might be expected for a bubble around a single source galaxy (Wyithe & Loeb 2005). Note also that $R_{\rm eff}$ is much greater than the typical radius $\bar{R}$ of a bubble if the distribution is wide. However, dense absorbers such as Lyman limit systems that are found to be associated with galaxies in simulations could restrict the size of bubbles (Gnedin & Fan 2006; Kohler & Gnedin 2007). Furthermore, near the beginning of reionization the existing bubbles should be much smaller in radius.

To make these considerations concrete, we examine the analytic model of Furlanetto et al. (2004) which makes specific predictions for the bubble distribution when coupled with the simulations of Zahn et al. (2007) for the ionization history. Here reionization occurs fairly promptly and at low redshift. In this model, the peak radius of the size distribution is of order $\bar{R} \sim 1$ Mpc (comoving) early in reionization and increases to $\bar{R} \sim 10$-100 Mpc by the end of reionization (Furlanetto et al. 2006). The shape of the distribution shows some skewness toward smaller bubbles but can be crudely modelled by a log normal with a width that increases with redshift from $\sigma_{\ln R} \sim 0.5$ to $\sigma_{\ln R} \sim 1$. For simplicity we approximate this as a constant $\sigma_{\ln R} = 0.7$. Both the ionization history and the bubble distribution in this model act to lower the B-mode contributions as shown in Figure 11. They are several orders of magnitude below the lensing B-modes and would be relevant only if the polarization field were cleaned of lensing on the whole sky. This model can also be considered near the minimal expected contribution in that the total optical depth is quite low ($\tau_* = 0.055$) and the duration of reionization quite short.

The model in Figure 11 illustrates some exceptions to our earlier conclusions. Because x_e and $R_{\rm eff}$ change rapidly with redshift, the redshift-averaged effective radius is not necessarily well approximated by $R_{\rm eff}(0.8z_i)$ as described in Section 4.2. The location of the peak at $\ell_{\rm peak} \sim 400$ indicates that the main contribution is from bubbles with radii $R \sim 50$ Mpc, and $R_{\rm eff}$ does not reach this size until around $z = 7$. Related to this is the fact that in this model, nearly all of the B-mode power comes from bubbles at $z \lesssim 7$, at the very end of reionization. In the models we examined where reionization is a more gradual process, a large fraction of the power comes instead from the highest-redshift bubbles.

Our model assumes that high-density regions that host ionizing sources are ionized before areas with lower density, consistent with recent simulations of reionization (e.g., Cen 2003; Sokasian et al. 2004; Iliev et al. 2006; Gnedin & Fan 2006; Zahn et al. 2007). Mod-

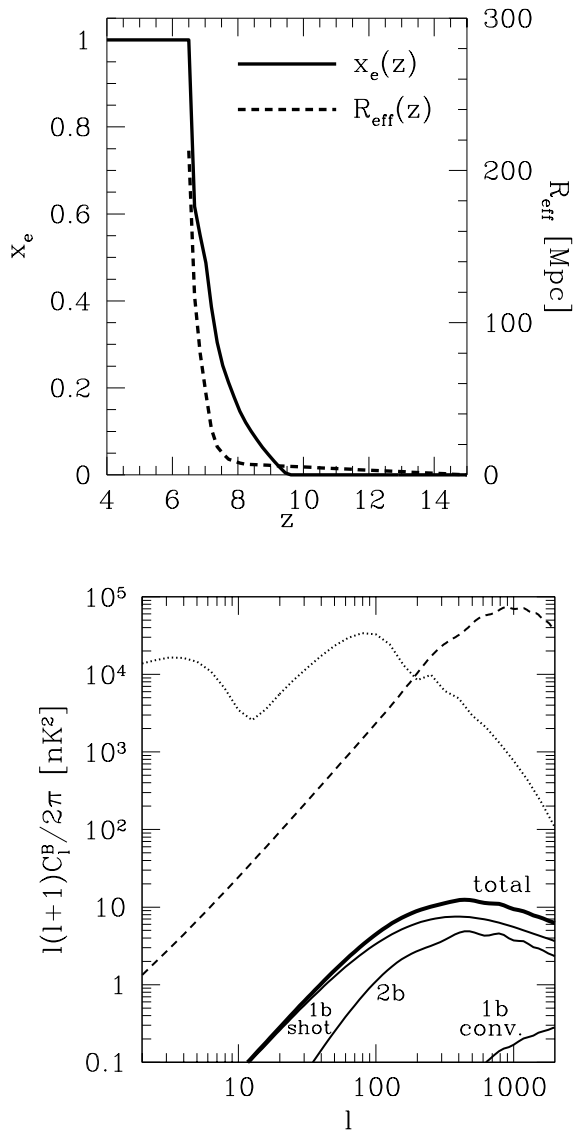

FIG. 11.— Ionization history and bubble size (*upper panel*) and B polarization from inhomogeneous reionization (*lower panel*) for a model intended to approximate the results of the reionization simulations of Zahn et al. (2007). The width of the bubble size distribution is chosen to be $\sigma_{\ln R} = 0.7$. As in Figure 4, the lensing B-modes (*dashed*) and gravitational wave B-modes (*dotted*) are shown for comparison. The components of the inhomogeneous reionization power spectrum are also plotted as in Figure 4. The total optical depth for this model is $\tau_* = 0.055$ and the duration of reionization is fairly short so this model can be taken as nearly the minimal B-modes from inhomogeneous reionization.

els in which reionization proceeds in the reverse order have also been proposed, and such a scenario could produce different B-mode spectra from those studied here (Miralda-Escudé et al. 2000). If reionization does begin in voids, we would expect the two-bubble contribution to the B polarization to be affected the most. As long as the H II regions in such a scenario could still be characterized as roughly spherical ionized regions with a size distribution that is approximately log normal, our model should still be sufficient to describe the shot noise contribution to the B-modes.

6. DISCUSSION

We have presented a comprehensive study of the generation of B-mode polarization by inhomogeneous reionization with an emphasis on the phenomenological properties required to generate a substantial contamination for degree scale gravitational wave studies. We base our study on a general parameterization of inhomogeneous reionization in terms of three functions of redshift: the mean ionization fraction, the effective bubble radius, and the width of a log normal radius distribution.

We find that these B-modes are only important when the ionized bubbles are sufficiently rare that the power spectrum is dominated by the shot noise of the bubbles. In such models, the B-modes are maximized by taking an effective bubble radius as large as possible, up to a few hundred Mpc, at as high a redshift as possible for a total duration of reionization that is as long as possible, while still remaining consistent with constraints on the total optical depth. The width of the bubble distribution is less critical but a wider distribution can make the effective bubble radius much larger than the typical bubble. The details of the ionization history are also less relevant so long as a finite ionization fraction remains at high redshift. We provide useful scaling relations for estimating the B-mode contributions for a wide variety of scenarios.

These conditions are constrained both observationally and by theoretical expectations. A substantial ionization fraction at high redshift would violate the shape of the observed E-mode power spectrum which sets a maximum redshift of $z \sim 30$. A large bubble radius would produce an large optical depth through its center and hence inhomogeneous obscuration of the acoustic peaks. Combined these conditions still allow power at $\ell = 100$ that is ~ 5 times the power produced by gravitational lensing or ~ 0.1 μK in the polarization field. These amplitudes can be reached for example by ~ 140 Mpc bubbles at $z \sim 30$. This level is also comparable to the *maximum* allowed B-modes from gravitational waves at $\ell = 100$. On the other hand, not even these models would predict B-modes at $\ell \lesssim 10$ that would mask the maximal gravitational wave signal from reionization.

Current theoretical models and simulations would not predict the existence of such large ionization bubbles at such high redshifts. In these models bubbles grow to a few tens of Mpc only toward the end of a fairly prompt reionization. Nonetheless, even for conditions where the B-modes do not exceed the lensing signal, they can still be the leading order cosmological contaminant to the gravitational wave signal.

Even without de-lensing of the polarization, the well-defined power spectrum from lensing allows its contributions to be statistically subtracted, ultimately to the few percent level with a full-sky cosmic variance limited experiment. The uncertain form of the inhomogeneous reionization B-modes does not permit statistical subtraction. With $\tau_* = 0.12$, ~ 20 Mpc bubbles at $z \sim 15$ near the end of reionization would produce B-modes that are 1% of the power in lensing at $\ell = 100$ or 10% of the polarization field. Likewise with a lower total optical depth of $\tau_* = 0.06$, ~ 40 Mpc bubbles at $z \sim 10$ would produce the same effect. Such contributions would also be relevant for the percent precision measurements of

the lensing B-modes on smaller scales expected from the next generation of ground based experiments.

Acknowledgments: We thank S. DeDeo, O. Doré, N. Gnedin, D. Huterer, K.M. Smith, Y.S. Song, X. Wang and B. Winstein for useful conversations. MJM was supported by a National Science Foundation Graduate Research Fellowship. WH was supported by the KICP through the grant NSF PHY-0114422, the DOE through contract DE-FG02-90ER-40560 and the David and Lucile Packard Foundation.

REFERENCES

Alvarez, M. A., Shapiro, P. R., Ahn, K., & Iliev, I. T. 2006, ApJ, 644, L101, astro-ph/0604447
Barkana, R., & Loeb, A. 2001, Phys. Rep., 349, 125
Baumann, D., Cooray, A., & Kamionkowski, M. 2003, New Astronomy, 8, 565
Bock, J., et al. 2006, Final Report of the Task Force on Cosmic Microwave Background Research (Washington: Natl. Sci. Found.), astro-ph/0604101
Cen, R. 2003, Astrophys. J., 591, 12, astro-ph/0210473
Cooray, A., & Sheth, R. 2002, Phys. Rep., 372, 1
Fan, X., Carilli, C. L., & Keating, B. 2006, ARA&A, 44, 415, arXiv:astro-ph/0602375
Furlanetto, S. R., & Loeb, A. 2005, ApJ, 634, 1
Furlanetto, S. R., McQuinn, M., & Hernquist, L. 2006, MNRAS, 365, 115, arXiv:astro-ph/0507524
Furlanetto, S. R., Zaldarriaga, M., & Hernquist, L. 2004, ApJ, 613, 1, astro-ph/0403697
Gnedin, N. Y., & Fan, X. 2006, ApJ, 648, 1, arXiv:astro-ph/0603794
Gold, B., & Albrecht, A. 2003, Phys. Rev. D, 68, 103518
Gruzinov, A., & Hu, W. 1998, ApJ, 508, 435, astro-ph/9803188
Hansen, F. K., Banday, A. J., & Górski, K. M. 2004, MNRAS, 354, 641, astro-ph/0404206
Hirata, C. M., & Seljak, U. 2003, Phys. Rev., D67, 043001, astro-ph/0209489
Hu, W. 2000, ApJ, 529, 12, astro-ph/9907103
Hu, W., & Okamoto, T. 2002, ApJ, 574, 566, astro-ph/0111606
Iliev, I. T., Mellema, G., Shapiro, P. R., & Pen, U.-L. 2006, ArXiv Astrophysics e-prints, astro-ph/0607517
Kamionkowski, M., Kosowsky, A., & Stebbins, A. 1997, Physical Review Letters, 78, 2058
Kesden, M., Cooray, A., & Kamionkowski, M. 2002, Phys. Rev. Lett., 89, 1304
Knox, L., Scoccimarro, R., & Dodelson, S. 1998, Physical Review Letters, 81, 2004
Knox, L., & Song, Y.-S. 2002, Phys. Rev. Lett., 89, 011303, astro-ph/0202286
Kohler, K., & Gnedin, N. Y. 2007, ApJ, 655, 685, arXiv:astro-ph/0605032
Liu, G.-C., Sugiyama, N., Benson, A. J., Lacey, C. G., & Nusser, A. 2001, ApJ, 561, 504
Miralda-Escudé, J., Haehnelt, M., & Rees, M. J. 2000, ApJ, 530, 1, astro-ph/9812306
Page, L. et al. 2006, ArXiv Astrophysics e-prints, astro-ph/0603450
Santos, M. G., Cooray, A., Haiman, Z., Knox, L., & Ma, C.-P. 2003, ApJ, 598, 756
Seljak, U., & Hirata, C. M. 2004, Phys. Rev. D, 69, 043005
Seljak, U., & Zaldarriaga, M. 1997, Physical Review Letters, 78, 2054
Sheth, R. K., & Tormen, G. 1999, MNRAS, 308, 119, astro-ph/9901122
Sokasian, A., Yoshida, N., Abel, T., Hernquist, L., & Springel, V. 2004, Mon. Not. Roy. Astron. Soc., 350, 47, astro-ph/0307451
Spergel, D. N. et al. 2006, ArXiv Astrophysics e-prints, astro-ph/0603449
Valageas, P., Balbi, A., & Silk, J. 2001, A&A, 367, 1, astro-ph/0009040
Verde, L., Peiris, H. V., & Jimenez, R. 2006, Journal of Cosmology and Astro-Particle Physics, 1, 19
Wang, X., & Hu, W. 2006, ApJ, 643, 585, astro-ph/0511141
Weller, J. 1999, ApJ, 527, L1, astro-ph/9908033
Wyithe, J. S. B., & Loeb, A. 2003, Astrophys. J., 586, 693, astro-ph/0209056
Wyithe, J. S. B., & Loeb, A. 2005, ApJ, 625, 1, astro-ph/0407162
Zahn, O., Lidz, A., McQuinn, M., Dutta, S., Hernquist, L., Zaldarriaga, M., & Furlanetto, S. R. 2007, ApJ, 654, 12, arXiv:astro-ph/0604177
Zahn, O., Zaldarriaga, M., Hernquist, L., & McQuinn, M. 2005, ApJ, 630, 657
Zaldarriaga, M., & Seljak, U. 1998, Phys. Rev. D, 58, 023003